Phonon-Coupled High-Harmonic Generation for Exploring Nonadiabatic Electron-Phonon Interactions

Shi-Qi Hu,[1] Hui Zhao,[1] Xin-Bao Liu,[1] Qing Chen,[1,2] Da-Qiang Chen,[1,2] Xin-Yuan Zhang,[1,2] and Sheng Meng[1,2,3,*]

[1]*Beijing National Laboratory for Condensed Matter Physics and Institute of Physics, Chinese Academy of Sciences, Beijing 100190, People's Republic of China*

[2]*School of Physical Sciences, University of Chinese Academy of Sciences, Beijing 100049, People's Republic of China*

[3]*Songshan Lake Materials Laboratory, Dongguan, Guangdong 523808, People's Republic of China*

(Received 19 April 2023; revised 1 January 2024; accepted 26 August 2024; published 7 October 2024)

High harmonic generation (HHG) have received significant attention for the exploration of material properties and ultrafast dynamics. However, the lack of consideration for couplings between HHG and other quasiparticles, such as phonons, has been impeding the understanding of many-body interactions in HHG. Here, we reveal the many-body electron-phonon mechanism in the quasiparticle-coupled strong-field dynamics by investigating the nonadiabatic (NA) coherent-phonon-coupled HHG. Coherent phonons are revealed to effectively affect HHG via the adiabatic band modulation induced by phonon deformation effects and the NA and nonequilibrium distribution of photocarriers in multiple valleys. The adiabatic and NA mechanisms leave their fingerprint via influencing the phonon period and phase delay in the oscillation of HHG intensity, both of which are experimentally measurable. Investigation of these quantities enables the direct probing of the electron-phonon interaction in materials.

DOI: 10.1103/PhysRevLett.133.156901

High-harmonic generation (HHG) in solids represents a new frontier that has spurred numerous advances in attosecond science and strong-field condensed matter physics [1–5]. Recently, there has been considerable excitement regarding the exploration of material properties through this nonlinear laser-matter interaction [6–16]. Unfortunately, the quasiparticle effect, such as phonon dynamics on solid HHG is often ignored, despite the availability of laser-stimulated coherent phonons (CPs) [17–20] and the nonlinear phononics that play vital roles in material dynamics [21–24]. The rigid separation of the combined electron-nuclear dynamics hinders the further understanding of solid HHG mechanism and stands in stark contrast to gas-phase molecules, where the nuclear autocorrelation effects have been illuminated in HHG [25–27], leading to the modulation of the phase and amplitude of extreme ultraviolet emissions [28].

When the response time of phonon and electron is comparable, the electron-phonon interaction (EPI) and its nonadiabatic (NA) effects become vital [29,30]. Moreover, given the phonon deformations (PDs) alter the electron potential, the Goldstone-Higgs mode coupling [31–33] may introduce spontaneous symmetry breaking and provide additional channels for electron excitation. Given that solid HHG typically occurs in the presence of phonons, CP-coupled HHG provides a representative example for exploring particle-quasiparticle coupled dynamics and has demonstrated significant phonon modulations on the time-dependent HHG recently [34–38]. However, the NA EPI mechanism behind phonon-coupled HHG, and thus the direct probing of the EPI—one of the most crucial interactions in solids—and its nonadiabaticity is still lacking.

In this Letter, the NA dynamics of coherent-phonon-coupled HHG in the two-dimensional transition-metal dichalcogenide MoS_2 is investigated. We find that (i) the oscillation of HHG yield with the phonon period is attributed to the adiabatic modulation of the band structure induced by PD. (ii) The observed phase delay between the oscillation of harmonic yield and phonon motion originates from the NA dynamics of photoexcited carriers in multiple valleys. (iii) We propose the concept of directly probing the EPI and its nonadiabaticity through analysis of the CP-coupled HHG spectroscopy.

Our study is performed using the time-dependent *ab initio* package based on the real-time time-dependent density-functional theory (TDDFT) [39–41], which naturally includes the NA feedback beyond the Born-Oppenheimer approximation between electrons and phonons through evolving both of them simultaneously. The laser pulses used to excite the CPs and probe the HHG are linearly polarized with a time-dependent electric field $\boldsymbol{F}(t) = \boldsymbol{F}_0 \cos(\omega t) \exp(-(t-t_0)^2)/2\sigma^2)$ and σ is the pulse duration. The HHG spectra are obtained by the Fourier transform of photocurrent $\boldsymbol{j}(t) = (1/2i) \int dr[\psi^*(r,t)\nabla\psi(r,t) + \text{c.c.}]$, i.e., $\text{HHG}(\omega) = |\int \omega \boldsymbol{j}(t) \exp(-i\omega t) dt|^2$. More details on the computation methodology can be found in the Supplemental Material [41].

*Contact author: smeng@iphy.ac.cn

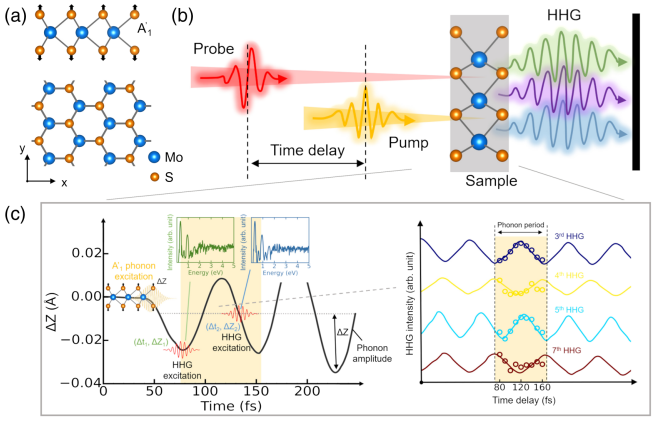

FIG. 1. (a) The atomic structure and A_1' phonon mode of monolayer MoS_2. (b) Schematics showing the pump-probe setup for CPs and HHG. (c) The CPs are excited and subsequently probed by the HHG at a different pump-probe delay. The HHG spectra and HHG yields oscillating with time are also shown. The yellow shadow shows the HHG dynamics during a phonon period.

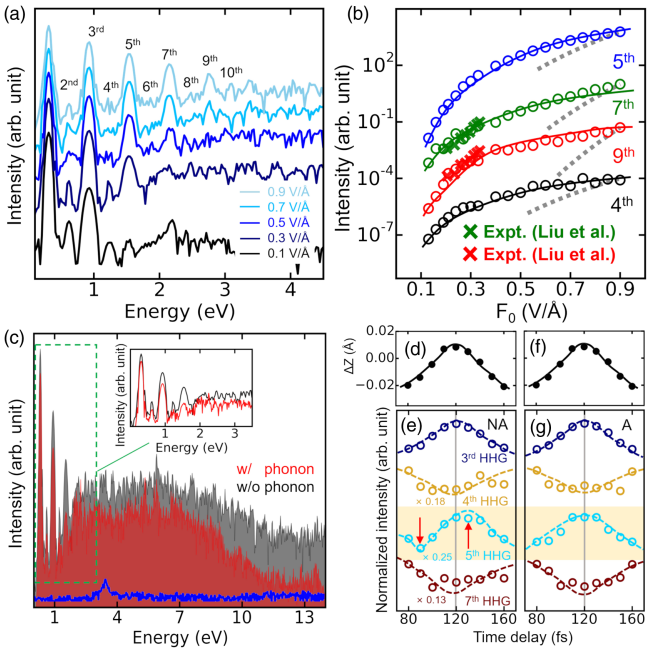

FIG. 2. (a) The HHG spectra without A_1' CPs under a different laser field. (b) The HHG intensity as a function of laser field without CPs. The dashed gray lines denote the perturbative nonlinear response $I_n \sim F_0^{2n}$. The crosses represent the experimental data in Ref. [42]. (c) The HHG spectra without (black) and with (red) A_1' CPs. The blue line shows the signal of the pump laser. (d) and (f) The ΔZ of A_1' CPs in one phonon period. The oscillation of HHG intensity in one phonon period within NA (e) and adiabatic (g) framework. The dashed lines are a guide to the eyes. The yellow shadow shows the harmonic with a phase delay compared to the ΔZ, and the phase delay is labeled by the red arrows. The probe laser strength used in (c)–(g) is ~0.3 V/Å.

The setup of phonon-coupled HHG is shown in Figs. 1(b) and 1(c), where a ~3.0 eV, $\sigma \sim 20$ fs pump pulse with peak field strength of 0.09 V/Å, polarization along zigzag direction is used to excite CPs in monolayer MoS_2; then subsequently an intense IR laser pulse (~0.3 eV, $\sigma \sim 20$ fs) is applied to probe the phonon dynamics by generating HHG. The polarization of probe laser electric field is along the armchair direction ($\mathbf{\Gamma} - \mathbf{K}$ direction). The photon energy of pump and probe lasers we used here is identical to recent experiments [17,42].

Figure S1 of Supplemental Material shows the laser-induced CPs of monolayer MoS_2 [41]. The pump laser primarily induces the A_1' mode with the S atom displaced out of plane by $\Delta \boldsymbol{Z}$ [inset of Fig. 1(a)], which has an oscillation period ~78 fs, corresponding to a frequency ~420 cm^{-1}, showing a near consistency with the experimental observation [the period ~82 fs and frequency ~405 cm^{-1}, the dashed line in Fig. S1(b)] [17]. The resultant maximum atomic displacement is ~0.02 Å.

With no phonon vibrations (fixed lattice), Figs. 2(a) and 2(b) display the HHG spectra and harmonic intensity as a function of field intensity of probe laser $\boldsymbol{F}_0$, which shows good agreement with the previous experimental measurements [41]. Given that the photon energy of the probe laser (~0.3 eV) is much lower than the MoS_2 band gap (~1.8 eV), as previously investigated [42], the harmonics [e.g., the third to seventh HHG (0.9–2.1 eV)] we focus on primarily originate from the intraband mechanism [12,43] of the first conduction band (CB).

This conclusion is further supported by the dominant contribution of the intraband dynamics to HHG spectra, and the consistency of the doping and field dependence of HHG between the TDDFT and intraband model results (Figs. S2 and S3 of the Supplemental Material [41]), as well as the time-frequency HHG spectrograms [Fig. S5(b) [41]], where low-order third to seventh harmonics are generated at the peak of the electric field with no chirp [4,11,44].

With A_1' CPs pumped, aligning with the recent study [34], the CP-coupled HHG spectra become noisy and less frequency-comb-like, suggesting the interference of electron dynamics due to the interaction with CPs.

The influence of CPs dynamics on the HHG process can be controlled by adjusting the pump-probe time delay [Fig. 1(a)] [34,35]. With the excitation of A_1' CPs, we intentionally vary the delay time of the probe laser from ~80 fs to ~160 fs, corresponding to one phonon period and then investigate the time-dependent HHG. Considering the weak intensity, different photon energy, and polarization, the phonon pump laser has almost no effects on the HHG process [the blue line in Fig. 2(b)].

As shown in Figs. 2(d) and 2(e), two characteristics of the time-dependent HHG coupled with A_1' CPs are evident alongside the phonon displacements $\Delta \boldsymbol{Z}$ within one phonon period: (i) the HHG yield for each order oscillates periodically with the CPs; and (ii) an obvious phase delay

(∼10 fs) is observed for fifth harmonic oscillation compared to the $\Delta \boldsymbol{Z}$.

According to the semiclassical intraband model (IM), the electrons are excited at the minimum of the conduction band (the **K** valley), and undergo laser-driven Bloch oscillation in the band. HHG can be generated through scattering with the nonlinearity of the band. For a laser field with frequency ω and strength $\boldsymbol{F}_0$, the HHG intensity can be represented as [12,41,43]

$$I_n \propto \rho(n\omega)^2 \left| \sum_{m=1}^{m_{\max}} ma\beta_m J_n\left(\frac{me\boldsymbol{F}_0 a}{\hbar\omega}\right) \right|^2, \tag{1}$$

where β_m is the Fourier coefficients of band dispersion $\varepsilon(\boldsymbol{k}) = \sum_{m=0}^{m_{\max}} \beta_m \cos(m\boldsymbol{k}a)$ (a is lattice constant and m is lattice site index) [12,16]. ρ is carrier population; J_n is n order Bessel function of the first kind.

The phonon period and the phase delay of the oscillation of HHG intensity primarily stem from the adiabatic modulation of band dispersion β_m and the NA effects of ρ, respectively. For β_m, the modulation is induced by the PD (such as bond compression/stretching) via EPI.

For phonon displacement oscillating with frequency Ω, $\Delta \boldsymbol{Z} \sim \boldsymbol{Z}_0 e^{i\Omega t}$, the band modulation relies on the EPI matrix element g_{ii} adiabatically: $\varepsilon(\boldsymbol{k}, t) = \varepsilon_0(\boldsymbol{k}) + g_{ii}(\boldsymbol{k})\Delta \boldsymbol{Z}(t)$, ε_0 is the original band energy at $\Delta \boldsymbol{Z} = 0$. With the tight-binding framework, $\varepsilon(\boldsymbol{k}, t) = \sum_{m=0}^{m_{\max}} \beta'_m(t) \cos(m\boldsymbol{k}a) = \sum_{m=0}^{m_{\max}} [\beta_{m,0} + \gamma_m \Delta \boldsymbol{Z}(t)] \cos(m\boldsymbol{k}a)$ and thus HHG intensity $I_n(t) \propto \rho(n\omega)^2 |\sum_{m=1}^{m_{\max}} ma[\beta_{m,0} + \gamma_m \Delta Z(t)] J_n(meF_0 a/\hbar\omega)|^2$, where $\beta_{m,0}$ and γ_m are Fourier coefficients of $\varepsilon_0(\boldsymbol{k})$ and $g_{ii}(\boldsymbol{k})$, respectively.

The Fourier coefficients $\beta'_m(t) = \beta_{m,0} + \gamma_m \Delta \boldsymbol{Z}(t)$ and HHG intensity oscillates synchronously with $\Delta \boldsymbol{Z}(t)$ and have the same phonon period [41]. This scenario is supported by the consistent phonon period observed in the oscillation of HHG intensity, obtained by the adiabatic Born-Oppenheimer (labeled as A) dynamics, as well as the IM of the first CB where the modulation of ρ is excluded [Fig. 2(g) and Fig. S4 of the Supplemental Material [41]].

On the other hand, both the adiabatic dynamics and the IM fail to reproduce the phase delay between the oscillation of the fifth harmonic and PD, implying a NA EPI mechanism of photocarrier population ρ. By tracking the laser field quasimomentum $\boldsymbol{k}_A(t) = [(-e)/\hbar] \int \boldsymbol{F}(t')dt'$ applied on electrons in reciprocal space during the generation time of HHG (Fig. S5 of Supplemental Material [41]), the fifth HHG dynamics is revealed to occur around the **Σ** valley.

Figure 3 and Fig. S6 of the Supplemental Material [41] show the NA behavior of ρ on the first CB within **K** and **Σ** valleys. During HHG, the laser-driven population forms a time-dependent nonequilibrium distribution. When the S atom displacement out of plane is compressed (stretched) along the A_1' phonon eigenvector, the band energy of **Σ** valleys is reduced (enhanced), and thus the ρ at **Σ** increases (decreases) [Figs. 3(a), 3(b), and 3(d)].

In adiabatic regime (labeled by A), the carriers can fully respond to phonons and move together with the band, resulting in simultaneous population changes of carriers at the **Σ** valley alongside the PD. However, in NA regime, the carriers lag behind the phonon motion, causing a delay between carrier population dynamics and the band modulation. For the same stretched (compressed) band structures, the carrier distribution at **Σ** valley in the NA regime is higher (lower) than that in the adiabatic regime, leading to a significant residual (deficiency) of carrier population differences $\Delta\rho = \rho_{\mathrm{A}} - \rho_{\mathrm{NA}}$ between adiabatic and NA frameworks [Figs. 3(c) and 3(e)].

The adiabatic and NA dynamics of the photocarrier is further validated by the population at **K** and **Σ** valleys changing along with $\Delta \boldsymbol{Z}(t) \sim \boldsymbol{Z}_0 e^{i\Omega t}$ [Figs. 3(g) and 3(h)]. For **K** valley, the carriers oscillate adiabatically and simultaneously with PD, while for **Σ** valley, a ∼10 fs NA delay identical with the fifth HHG, τ is observed.

At initial time t_0, the photocarriers are excited from the valence band to the CB. The population $\rho(t)$ on the ith CB, which can be represented by the occupation coefficient c_i, i.e., $\rho(t) = |c_i(t)|^2$. After that, the carriers generate HHG via the laser-driven Bloch oscillations modulated by CPs via NA EPI.

According to the NA dynamics theory [45], the carrier occupation $i\hbar(\partial/\partial t)c_i = c_i\varepsilon_i - i\hbar \sum_j \kappa_{ij} \dot{\boldsymbol{R}} c_j$. $\dot{\boldsymbol{R}}$ is the nucleus velocity, ε_i and ε_j are eigenvalues of the ith and jth electron states. κ_{ij} is proportional to the EPI matrix element and describes the NA coupling between electron and nucleus, which explains the huge nonadiabaticity at **Σ** valley.

In the adiabatic framework, $\kappa_{ij} = 0$, $c_i(t) \propto c_i(t = t_0) \times \exp[i \int_{t_0}^{t} \varepsilon_i[\boldsymbol{R}(t')]dt']$ and thus $\rho(t) \propto |c_i(t = t_0)|^2$, which only depends on the photocarrier population $\rho(t_0)$ at initial time t_0. Similar to Zener tunneling [46], $\rho(t_0)$ is proportional to the transition rate, and thus relies exponentially on the band gap ε_G, which is adiabatically dependent on phonon displacement $\Delta \boldsymbol{Z} \sim \boldsymbol{Z}_0 e^{i\Omega t}$ via the EPI matrix element g_G between the valence band and CB, i.e., $\varepsilon_G \propto \varepsilon_G^0 + g_G \Delta \boldsymbol{Z}$. Therefore, $\rho(t_0) \propto \exp[-\sqrt{\varepsilon_G}] \propto \exp\left[-\sqrt{\varepsilon_G^0 + g_G \Delta \boldsymbol{Z}}\right]$ ρ oscillates synchronously with $\Delta \boldsymbol{Z}$, there is no NA time delay.

On the other hand, in NA case, $\rho(t) = \int_{t_0}^{t} \sum_j \kappa_{ij} \dot{\boldsymbol{R}} \times (c_i^* c_j + c_j^* c_i)dt'$. Considering the lattice configuration $\boldsymbol{R}(t) \sim \boldsymbol{Z}_0 e^{i\Omega t}$ and thus $\dot{\boldsymbol{R}} \sim \Omega \boldsymbol{Z}_0 e^{i[\Omega t + (\pi/2)]}$, the relationship $e^{i[\Omega t + (\pi/2)]} + e^{i\Omega t} = 2\sqrt{2} e^{i[\Omega t + (\pi/4)]}$ gives $\rho(t) \propto -\sum_j \kappa_{ij} \boldsymbol{Z}_0 e^{i[\Omega t + (\pi/4)]}$ [41]. The nonadiabaticity yields a $\pi/4$ phase shift on $\rho(t)$ oscillation. For A_1' mode phonon with an oscillation period ∼80 fs, the $\pi/4$ phase shift corresponds to a $\tau \sim 10$ fs delay time (i.e., $[(\pi/4)/2\pi] = (\tau/80)$), agreeing well with the TDDFT results [41].

For the HHG contributed by the photocarrier at **Σ** valley, the NA population $\rho_\Sigma \propto -\Sigma_j g_{ij} \boldsymbol{Z}_0 e^{i\Omega[t + (\pi/4)]}$ provides the

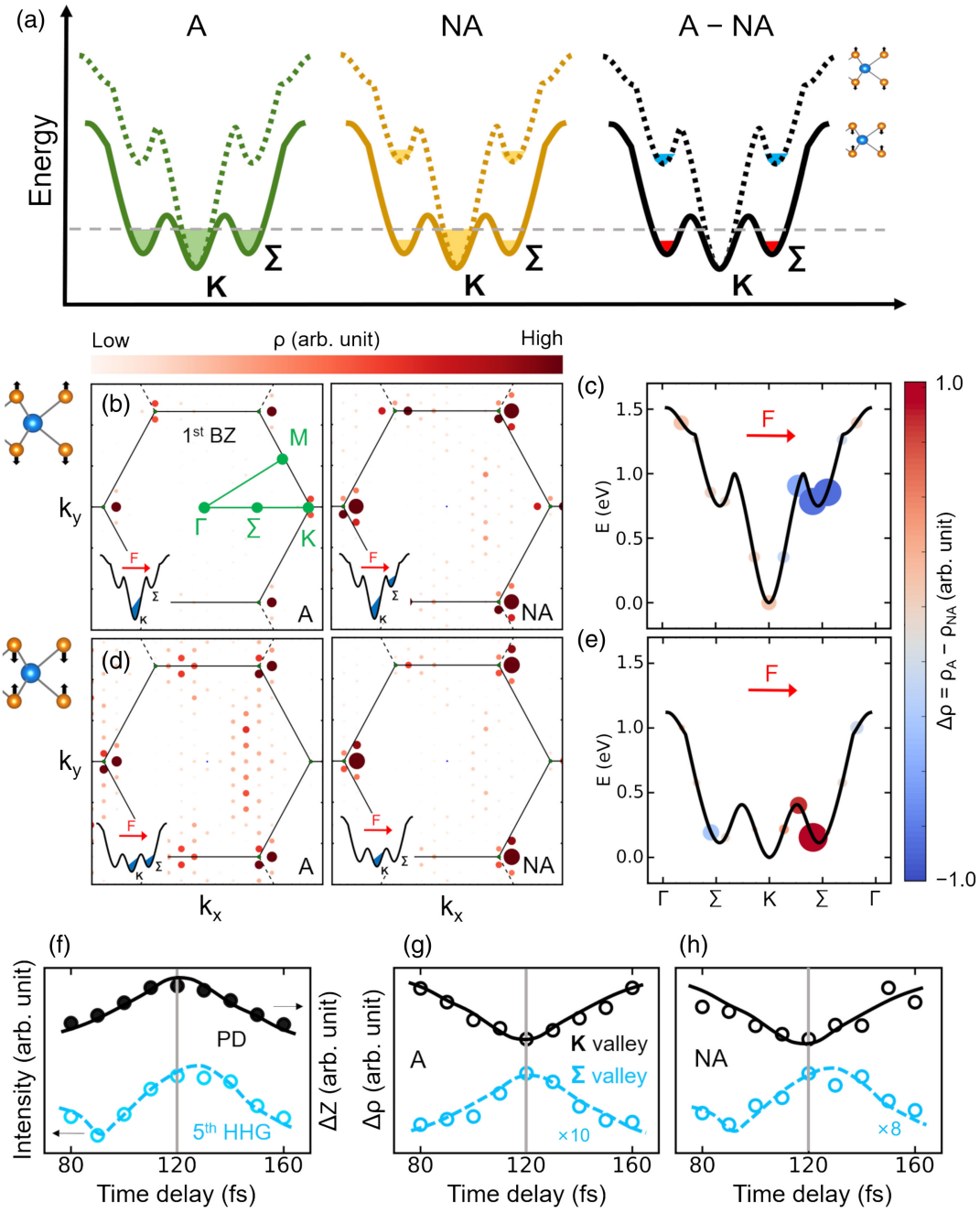

FIG. 3. (a) Schematic of band structure and photocarrier distribution (regions with color shades) of first CB in the adiabatic (green color) and NA (yellow color) regimes and the difference between them. The red (blue) color shades in the right panel label the increase (decrease) of population deducting the NA cases from adiabatic cases, respectively. The solid (dashed) lines represent the compression (stretching) band structure displaced along the A_1' eigenvectors. The photocarrier population at the laser field peak time of the first CB in adiabatic (left) and NA (right) cases with the stretching (b) and compression (d) band structure. $\Delta\rho$ with the stretching (c) and compression (e) band structure. The red arrows label the laser polarization. The color and size of circles mark the sign and the number of populations. (f) ΔZ of A_1' CPs and the fifth HHG oscillation within NA framework within one phonon period. The population at K and $\boldsymbol{\Sigma}$ valleys changing with ΔZ within adiabatic (g) and NA framework (h).

harmonic intensity an additional time delay with respect to $\Delta \boldsymbol{Z}(t)$ by $I_n \propto \rho_\Sigma |\sum_{m=1}^{m_{\max}} ma\beta_m J_n(me\boldsymbol{F}_0 a/\hbar\omega)|^2 \sim e^{i[\Omega t+(\pi/4)]} \sim e^{i\Omega t+\tau}$, which explains well the time delay observed in the oscillation of the fifth harmonic.

Although intraband HHG is used to show the NA time delay here, $c_i(t)$ manifests itself in both the intraband and interband HHG through the carrier population $\rho(t) \sim c_i^*(t)c_i(t)$ and transition dipole moment

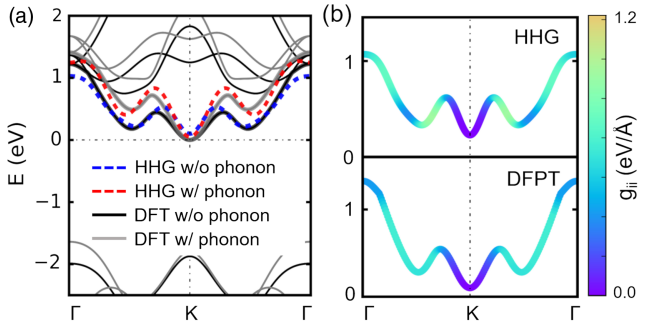

FIG. 4. (a) The band structure along $\Gamma - \mathrm{K}$ direction without and with PD, obtained from the density-functional theory and HHG reconstruction. The first CB minimum without PD is set to 0 eV and used as an energy benchmark. (b) The distribution of the EPI matrix element g_{ii} along $\Gamma - \mathrm{K}$ direction.

$P_{ij}(t) \sim c_i^*(t)c_j(t)$. Consequently, the NA effects [47–50], persistent also in interband HHG oscillation, are independent of the HHG mechanism [41,51,52]. A similar phenomenon is also observed in recent work [34] without a clear explanation.

We finally propose the phonon-coupled HHG spectra as an all-optical approach to detect the EPI. According to the definition of the EPI matrix element of the ith band g_{ii} [53,54], g_{ii} can be described by the first derivative of the band energy ε_i with respect to phonon displacement $\Delta\boldsymbol{Z}(t)$, i.e., $g_{ii} = \partial\varepsilon_i/\partial\boldsymbol{Z} = \Delta\varepsilon_i/\Delta\boldsymbol{Z}$ [53,54]. For a certain $\Delta\boldsymbol{Z}$ [55–58], the g_{ii} relies on the measurement of band change $\Delta\varepsilon_i = \varepsilon_i(t_1) - \varepsilon_i(t_2)$.

As shown in Eq. (1), the band coefficients β_m can be obtained by fitting the field dependence of the intensity of phonon-phase-matched HHG at different delay times t_1 and t_2, which is successfully used to retrieve the band dispersion with static lattice in various materials [10,12,16]. Then g_{ii} scales with $g_{ii}(\boldsymbol{k}) \propto \sum_{m=0}^{m_{\max}} \beta_m(t_1)\cos(m\boldsymbol{k}a) - \sum_{m=0}^{m_{\max}} \beta_m(t_2)\cos(m\boldsymbol{k}a)$.

Following the above strategy, by fitting the field dependence of the third and seventh harmonics at 80 and 120 fs with different $\Delta\boldsymbol{Z}$, the dispersion of the first CB along $\boldsymbol{\Gamma - K}$ without or with A_1' PD, as well as the EPI matrix element g_{ii} of A_1' mode, is reconstructed in MoS_2 in Figs. 4(a) and 4(b). The bands and g_{ii} distribution reconstructed from the phonon-coupled HHG agree well with that obtained from density functional theory and density functional perturbation theory, demonstrating the effectiveness of the present approach.

Acknowledgments—We acknowledge financial support from MOST (Grant No. 2021YFA1400200), NSFC (Grants No. 12025407, No. 92250303, and No. 11934003), and CAS (No. YSBR047 and No. XDB330301). S.-Q. H. acknowledges financial support from NSFC (No. 12304096), China Postdoctoral Science Foundation (2022TQ0362), and Special Research Assistant of the Chinese Academy of Sciences Foundation.

Data availability—The data that support the findings of this study are available from the contact author upon reasonable request.

S. M. conceived and supervised the project. S.-Q. H., X.-Y. Z. performed the theoretical modeling and TDDFT calculations. D.-Q. C and Q. C. contributed to the software code. S.-Q. H., H. Z., X.-B. L., and S. M. analyzed the data. The manuscript was written by S.-Q. H. and S. M.

The authors declare no competing financial or non-financial interests.

[1] F. Krausz and M. Ivanov, Attosecond physics, Rev. Mod. Phys. **81**, 163 (2009).
[2] S. Y. Kruchinin, F. Krausz, and V. S. Yakovlev, Colloquium: Strong-field phenomena in periodic systems, Rev. Mod. Phys. **90**, 021002 (2018).
[3] T. Higuchi, M. I. Stockman, and P. Hommelhoff, Strong-field perspective on high-harmonic radiation from bulk solids, Phys. Rev. Lett. **113**, 213901 (2014).
[4] M. Wu, S. Ghimire, D. A. Reis, K. J. Schafer, and M. B. Gaarde, High-harmonic generation from Bloch electrons in solids, Phys. Rev. A **91**, 043839 (2015).
[5] G. Vampa, C. R. McDonald, G. Orlando, P. B. Corkum, and T. Brabec, Semiclassical analysis of high harmonic generation in bulk crystals, Phys. Rev. B **91**, 064302 (2015).
[6] H. Lakhotia, H. Y. Kim, M. Zhan, S. Hu, S. Meng, and E. Goulielmakis, Laser picoscopy of valence electrons in solids, Nature (London) **583**, 55 (2020).
[7] Y. You, D. Reis, and S. Ghimire, Anisotropic high-harmonic generation in bulk crystals, Nat. Phys. **13**, 345 (2017).
[8] Y. Bai, F. Fei, S. Wang, N. Li, X. Li, F. Song, R. Li, Z. Xu, and P. Liu, High-harmonic generation from topological surface states, Nat. Phys. **17**, 311 (2021).
[9] C. P. Schmid, L. Weigl, P. Grössing, V. Junk, C. Gorini, S. Schlauderer, S. Ito, M. Meierhofer, N. Hofmann, D. Afanasiev, J. Crewse, K. A. Kokh, O. E. Tereshchenko, J. Güdde, F. Evers, J. Wilhelm, K. Richter, U. Höfer, and R. Huber, Tunable non-integer high-harmonic generation in a topological insulator, Nature (London) **593**, 385 (2021).
[10] Y.-Y. Lv, J. Xu, S. Han, C. Zhang, Y. Han, J. Zhou, S.-H. Yao, X.-P. Liu, M.-H. Lu, H. Weng, Z. Xie, Y. B. Chen, J. Hu, Y.-F. Chen, and S Zhu, High-harmonic generation in Weyl semimetal β-WP_2 crystals, Nat. Commun. **12**, 6437 (2021).
[11] M. Garg, M. Zhan, T. T. Luu, H. Lakhotia, T. Klostermann, A. Guggenmos, and E. Goulielmakis, Multi-petahertz electronic metrology, Nature (London) **538**, 359 (2016).
[12] T. T. Luu, M. Garg, S. Yu. Kruchinin, A. Moulet, M. Th. Hassan, and E. Goulielmakis, Extreme ultraviolet high-harmonic spectroscopy of solids, Nature (London) **521**, 498 (2015).
[13] S. Ghimire and David A. Reis, High-harmonic generation from solids, Nat. Phys. **15**, 10 (2019).
[14] S. Ghimire, G. Ndabashimiye, A. D. DiChiara, E. Sistrunk, M. I. Stockman, P. Agostini, L. F. DiMauro, and D. A. Reis,

Strong-field and attosecond physics in solids, J. Phys. B **47**, 204030 (2014).
[15] G. Vampa, T. J. Hammond, N. Thiré, B. E. Schmidt, F. Légaré, C. R. McDonald, T. Brabec, D. D. Klug, and P. B. Corkum, All-optical reconstruction of crystal band structure, Phys. Rev. Lett. **115**, 193603 (2015).
[16] A. A. Lanin, E. A. Stepanov, A. B. Fedotov, and A. M. Zheltikov, Mapping the electron band structure by intraband high-harmonic generation in solids, Optica **4**, 516 (2017).
[17] C. Trovatello *et al.*, Strongly coupled coherent phonons in single-layer MoS_2, ACS Nano **14**, 5700 (2020).
[18] M. Hase, M. Kitajima, A. M. Constantinescu, and H. Petek, The birth of a quasiparticle in silicon observed in time-frequency space, Nature (London) **426**, 51 (2003).
[19] M. Hase, M. Katsuragawa, A. M. Constantinescu, and H. Petek, Frequency comb generation at terahertz frequencies by coherent phonon excitation in silicon, Nat. Photonics **6**, 243 (2012).
[20] A. von Hoegen, R. Mankowsky, M. Fechner, M. Först, and A. Cavalleri, Probing the interatomic potential of solids with strong-field nonlinear phononics, Nature (London) **555**, 79 (2018).
[21] R. Mankowsky, A. von Hoegen, M. Först, and A. Cavalleri, Ultrafast reversal of the ferroelectric polarization, Phys. Rev. Lett. **118**, 197601 (2017).
[22] T. F. Nova, A. S. Disa, M. Fechner, and A. Cavalleri, Metastable ferroelectricity in optically strained $SrTiO_3$, Science **364**, 1075 (2019).
[23] M. Först, C. Manzoni, S. Kaiser, Y. Tomioka, Y. Tokura, R. Merlin, and A. Cavalleri, Nonlinear phononics as an ultrafast route to lattice control, Nat. Phys. **7**, 854 (2011).
[24] A. S. Disa, T. F. Nova, and A. Cavalleri, Engineering crystal structures with light, Nat. Phys. **17**, 1087 (2021).
[25] M. Lein, Attosecond probing of vibrational dynamics with high-harmonic generation, Phys. Rev. Lett. **94**, 053004 (2005).
[26] S. Baker, J. S. Robinson, C. A. Haworth, H. Teng, R. A. Smith, C. C. Chirilă, M. Lein, J. W. G. Tisch, and J. P. Marangos, Probing proton dynamics in molecules on an attosecond time scale, Science **312**, 424 (2006).
[27] W. Li, X. Zhou, R. Lock, S. Patchkovskii, A. Stolow, H. C. Kapteyn, and M. M. Murnane, Time-resolved dynamics in N_2O_4 probed using high harmonic generation, Science **322**, 1207 (2008).
[28] A. Ferre *et al.*, Two-dimensional frequency resolved opto-molecular gating of high-order harmonic generation, Phys. Rev. Lett. **116**, 053002 (2016).
[29] E. Cappelluti, F. Caruso, and D. Novko, Properties and challenges of hot-phonon physics in metals: MgB2 and other compounds, Prog. Surf. Sci. **97**, 100664 (2022).
[30] K. Ishiok, M. Hase, M. Kitajima, L. Wirtz, A. Rubio, and H. Petek, Ultrafast electron-phonon decoupling in graphite, Phys. Rev. B **77**, 121402(R) (2008).
[31] M. Vallone, Structural phase transitions in crystals: phonons as Higgs and Goldstone excitations, Phys. Status Solidi (RRL) **14**, 2000265 (2020).
[32] M. Vallone, Higgs and Goldstone modes in crystalline solids, Phys. Status Solidi (b) **257**, 1900443 (2020).
[33] D. M. Juraschek, Q. N. Meier, and P. Narang, Parametric excitation of an optically silent Goldstone-like phonon mode, Phys. Rev. Lett. **124**, 117401 (2020).
[34] O. Neufeld, J. Zhang, U. D. Giovannini, H. Hübener, and A. Rubio, Probing phonon dynamics with multidimensional high harmonic carrier-envelope-phase spectroscopy, Proc. Natl. Acad. Sci. U.S.A. **119**, e2204219119 (2022).
[35] M. R. Bionta *et al.*, Tracking ultrafast solid-state dynamics using high harmonic spectroscopy, Phys. Rev. Res. **3**, 023250 (2021).
[36] Navdeep Rana, M. S. Mrudul, Daniil Kartashov, Misha Ivanov, and Gopal Dixit, High-harmonic spectroscopy of coherent lattice dynamics in graphene, Phys. Rev. B **106**, 064303 (2022).
[37] N. Rana and G. Dixit, Probing phonon-driven symmetry alterations in graphene via high-order-harmonic spectroscopy, Phys. Rev. A **106**, 053116 (2022).
[38] J. S. Ginsberg *et al.*, Phonon-enhanced nonlinearities in hexagonal boron nitride, Nat. Commun. **14**, 7685 (2023).
[39] S. Meng and E. Kaxiras, Real-time, local basis-set implementation of time-dependent density functional theory for excited state dynamics simulations, J. Chem. Phys. **129**, 054110 (2008).
[40] C. Lian, S. Hu, M. Guan, and S. Meng, Momentum-resolved TDDFT algorithm in atomic basis for real time tracking of electronic excitation, J. Chem. Phys. **149**, 154104 (2018).
[41] See Supplemental Material at http://link.aps.org/supplemental/10.1103/PhysRevLett.133.156901 for more details on computation methodology, HHG mechanism, and EPI probing by HHG.
[42] H. Liu, Y. Li, Y. S. You, S. Ghimire, T. F. Heinz, and D. A. Reis, High-harmonic generation from an atomically thin semiconductor, Nat. Phys. **13**, 262 (2017).
[43] M. Wegener, *Extreme Nonlinear Optics: An Introduction* (Springer, New York, 2005).
[44] M. Hohenleutner, F. Langer, O. Schubert, M. Knorr, U. Huttner, S. W. Koch, M. Kira, and R. Huber, Real-time observation of interfering crystal electrons in high-harmonic generation, Nature (London) **523**, 572 (2015).
[45] J. C. Tully, Nonadiabatic molecular dynamics, Int. J. Quantum Chem. **40**, 299 (1991).
[46] C. Zener, A theory of the electrical breakdown of solid dielectrics, Proc. R. Soc. A **145**, 523 (1934).
[47] S. Pisana, M. Lazzeri, C. Casiraghi, K. S. Novoselov, A. K. Geim, A. C. Ferrari, and F. Mauri, Breakdown of the adiabatic Born–Oppenheimer approximation in grapheme, Nat. Mater. **6**, 198 (2007).
[48] D. Novko, Broken adiabaticity induced by Lifshitz transition in MoS_2 and WS_2 single layers, Commun. Phys. **3**, 30 (2020).
[49] P. Garcia-Goiricelaya, J. Lafuente-Bartolome, I. G. Gurtubay, and A. Eiguren, Emergence of large nonadiabatic effects induced by the electron-phonon interaction on the complex vibrational quasiparticle spectrum of doped monolayer MoS_2, Phys. Rev. B **101**, 054304 (2020).
[50] E. Piatti, D. De Fazio, D. Daghero, S. R. Tamalampudi, D. Yoon, A. C. Ferrari, and R. S. Gonnelli, Multi-valley superconductivity in ion-gated MoS_2 layers, Nano Lett. **18**, 4821 (2018).
[51] N. Tancogne-Dejean, O. D. Mücke, F. X. Kärtner, and A. Rubio, Ellipticity dependence of high-harmonic generation in solids originating from coupled intraband and interband dynamics, Nat. Commun. **8**, 745 (2017).

[52] N. Yoshikawa, T. Tamaya, and K. Tanaka, High-harmonic generation in graphene enhanced by elliptically polarized light excitation, Science **356**, 736 (2017).

[53] F. Giustino, Electron-phonon interactions from first principles, Rev. Mod. Phys. **89**, 015003 (2017).

[54] G. Grimvall, *in The Electron-Phonon Interaction in Metals*, edited by E. Wohlfarth, Selected Topics in Solid State Physics (North-Holland, New York, 1981).

[55] S. Gerber *et al.*, Femtosecond electron-phonon lock-in by photoemission and x-ray free-electron laser, Science **357**, 71 (2017).

[56] S. Gerber, K. Kim, Y. Zhang *et al.*, Direct characterization of photoinduced lattice dynamics in $BaFe_2As_2$, Nat. Commun. **6**, 7377 (2015).

[57] X. Gu, X.-F., T. Furuhara, and W. Zhang, PTCLab: Free and open-source software for calculating phase transformation crystallography, J. Appl. Crystallogr. **49**, 1099 (2016).

[58] B. L. Henke, E. M. Gullikson, and J. C. Davis, X-ray interactions: Photoabsorption, scattering, transmission, and reflection at $E = 50–30,000$ eV, $Z = 1–92$. At. Data Nucl. Data Tables **54**, 181 (1993).